AD-A117 395 MILITARY ACADEMY WEST POINT NY F/G 19/1
MULTIPLE LAUNCH ROCKET SYSTEM (MLRS) FUZE.(U)
JUN 82 J J BERTIN, R L GOODYEAR

UNCLASSIFIED NL

END
DATE FILMED
8 82
DTIC

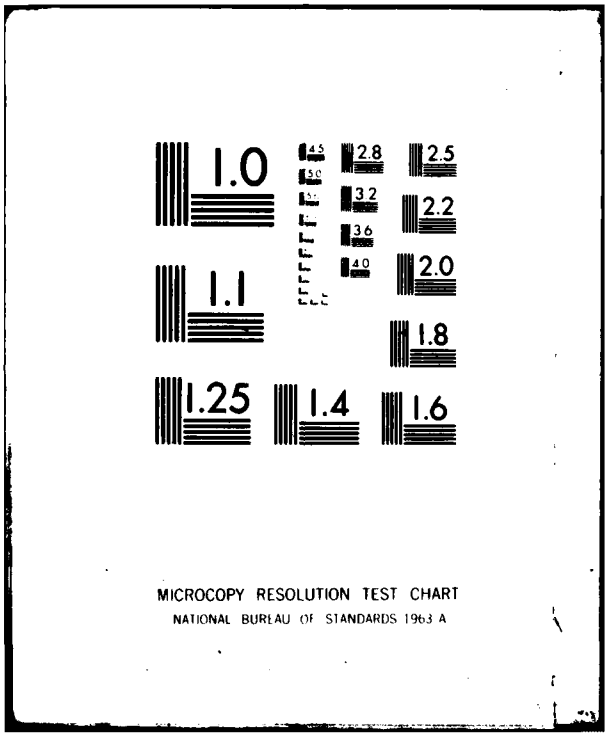
1.0
1.1
1.25
1.4
1.6
1.8
2.0
2.2
2.5
2.8
3.2
3.6
4.0
MICROCOPY RESOLUTION TEST CHART
NATIONAL BUREAU OF STANDARDS 1963 A

MULTIPLE LAUNCH ROCKET SYSTEM (MLRS) FUZE (U)

JOHN J. BERTIN, DR.
THE UNIVERSITY OF TEXAS AT AUSTIN
AUSTIN, TEXAS 78712
*RICHARD L. GOODYEAR, MAJ
U.S. MILITARY ACADEMY
WEST POINT, NEW YORK 10996

1. INTRODUCTION

When the U.S. Army began limited production of the fuze for the rocket warhead of the Multiple Launch Rocket System (MLRS), it was necessary to develop improved methods of testing fuzes as they came off the assembly line. Since the fuze contained a fluidic power supply that had never been type-classified, methods associated with previous battery-powered fuzes were inadequate for the production specification. Also during the validation and maturation phases of the development program, considerable testing in the laboratory, in wind tunnels, and in flight tests showed that laboratory tests in early specifications did not indicate adequately how a fuze would perform in actual flight. A key deficiency was the inability to duplicate in the laboratory the conditions near the summit of the rocket's trajectory. Operating the fluidic generator from an air source up to 14 kilopascals above atmospheric pressure approximated the expected pressure difference between the entrance and exit of the generator, but it failed to duplicate the effects of the air's speed.

The power supply project team at the U.S. Army Harry Diamond Laboratories (HDL) proposed a solution in the form of a relatively inexpensive high altitude chamber, which would duplicate both of these flight variables, and which could be incorporated into the fuze contractor's test equipment. Implementation of this proposal required a better understanding of the conditions of the air flow around the fuze ogive and through the generator. Consequently, HDL conducted a test program in the Aerodynamic Wind Tunnel at the Arnold Engineering Development Center. Test conditions included free-stream Mach numbers from 0.95 to 1.3 over a range of free-stream densities that simulated altitudes from 15.2 Km to 21 Km. The fuze ogive was instrumented with both static and pitot pressure probes, from which the pressure data were analyzed to describe the internal and external flow fields.

STAMP Security Classification here

BERTIN & GOODYEAR

2. EXPERIMENTAL PROGRAM

The general features of the nose cone are illustrated in the sketch presented in Figure 1. A sectioned drawing has been used to present the details of the external geometry and of the generator installation. The air that drives the fluidic generator enters the "inlet hole" in the stagnation region of the blunt face, passes through the generator assembly and into the (internal) chamber. It then flows through the exhaust ports into the (external) cavity. This use of the words "chamber" for the internal region and "cavity" for the depression in the external surface will be retained throughout this report. The 24 exhaust ports, which are 0.269 cm in diameter, are equally distributed circumferentially and are located in a shallow cavity that begins 3.259 cm ($x = 0.423\ x_o$) aft of the tip of the fuze. As shown in figure 1, x is the longitudinal position, as measured from the model nose. The reference length, x_o, was chosen to be 7.696 cm, the coordinate of the most-downstream pressure tap.

The nose cone used in the initial phase of the test program was instrumented with 29 surface pressure taps (or orifices), of which 21

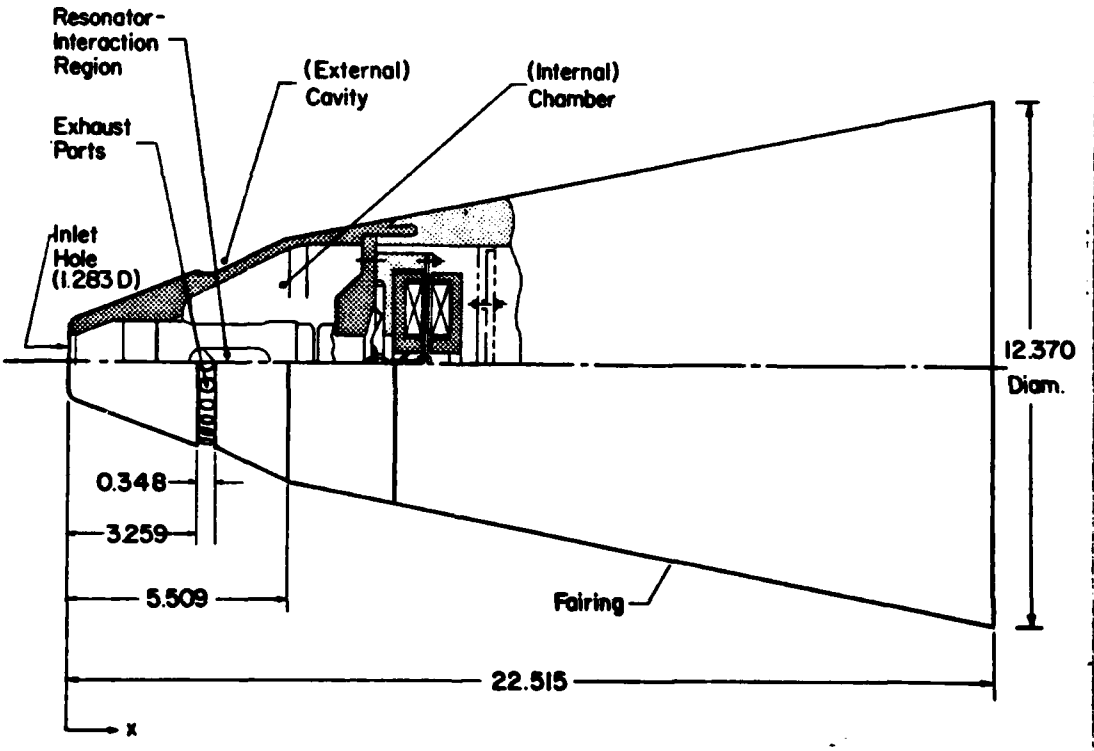

Figure 1. - Sketch of the Army/MLRS Fluidic-Generator Fuze-Assembly.

Codes /or Dist | Special

STAMP Security Classification here

were on the external surface and 8 were on the internal surface. The locations of the orifices for which data are presented in this paper are illustrated in Figure 2.

3. RESULTS

Static pressures and Pitot pressures were measured both on the external surface and on the internal surface of a full-scale fluidic generator/fuze assembly of the MLRS in the Aerodynamic Wind Tunnel (4T) at AEDC. The pressure data from these tests are discussed in this section.

3.1 External Pressures for 0° Angle of Attack

3.1.1 Pressures on Flat Face (x = 0.0)

A strong, detached shock wave forms in front of a blunt body when it is placed in a supersonic stream. The shape of the bow shock wave

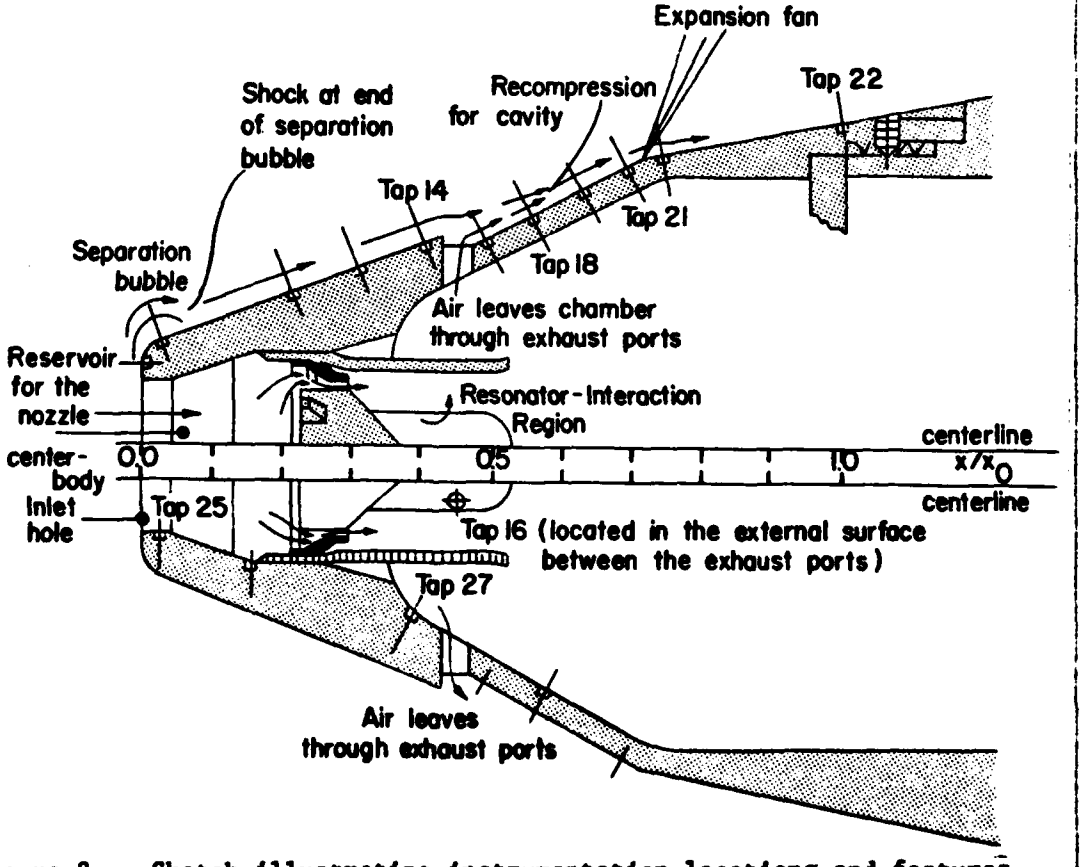

Figure 2. - Sketch illustrating instrumentation locations and features of proposed flow model.

for supersonic flow past the nose cone is shown in the schlieren photograph from a previous test program (1) that is presented in Figure 3. Since the Mach number of the flow represented by the schlieren photograph is greater than those of the present program, the stand-off distance of the bow shock wave is much less than would be the case for the present flows. This is to be expected. Nevertheless, the photograph provides valuable insights into the flow. Because the bow shock wave is curved, the static pressure on the surface should decrease from a value of the stagnation pressure downstream of a normal shock wave, p_{t2} , at the axis of symmetry to the sonic value at the corner. This pressure variation is illustrated by the pressure distribution that was presented elsewhere (2) for a free-stream Mach

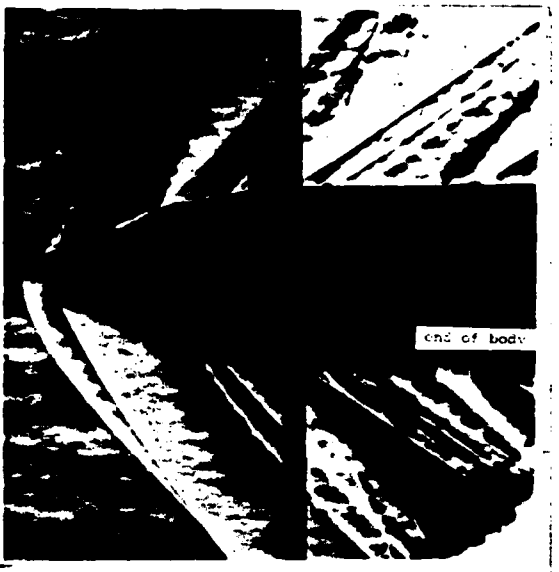

Figure 3. - Schlieren photograph from the tests of ref. 1, $M_\infty = 1.5$.

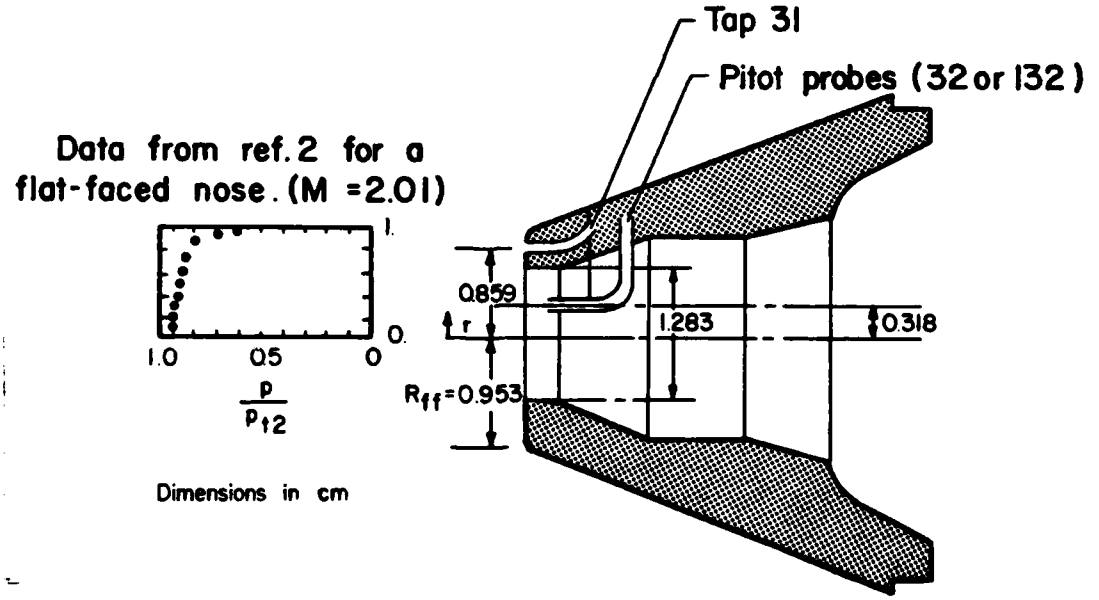

Figure 4. - Nose-region instrumentation and pressure distributions for a flat-faced cylinder (ref. 2).

number, M_∞, of 2.01 (see Figure 4). Although the presence of the inlet hole will modify the flow on the face of the fuze, the pressure distributions for the present tests will be similar to that of Figure 4 despite the difference in Mach number.

Included with the pressure distributions in Figure 4 are the pressure-instrumentation locations for two model variations tested. For selected tests a pitot probe was positioned in the inlet hole. There were two static-pressure orifices on the flat face of the nose cone, between the inlet hole and the corner radius. They were approximately 0.859 cm from the axis of symmetry, i.e., $r = 0.90\ R_{ff}$. The experimentally determined pressure coefficients, C_p, for orifice 31 are presented in Figure 5 at density altitudes (AD) of 18,290 m and 21,030 m. Included are the experimental values of C_p for the two total-pressure probes that were 0.318 cm from the axis, in the inlet hole. These experimentally determined C_p are compared with the theoretical C_p, as calculated for the flow downstream of a normal shock wave, using the relation:

$$C_{p,t2} = \left(\frac{p_{t2}}{p_\infty} - 1\right)\frac{2}{\gamma M_\infty^2}, \qquad (1)$$

where $C_{p,t2}$ is the stagnation pressure coefficient, p_∞ is free-stream static pressure, and γ is the ratio of specific heats. The ratio p_{t2}/p_∞ was determined as a function of M_∞ using normal shock wave tables (3).

The experimental values of C_p determined using the Pitot probes in the inlet hole are in very good agreement with the theoretical values. This is to be expected, since the probes are near the axis of symmetry (where the bow shock wave is most nearly normal) and, being Pitot probes, they provide a measure of the stagnation pressure. The surface static pressures at tap 31 are below the theoretical predictions. This is also to be expected. When a flat-faced cylinder with a "slender" conical afterbody is exposed to a supersonic stream, the bow shock wave is curved and the sonic "line" is fixed at the corner of the flat-

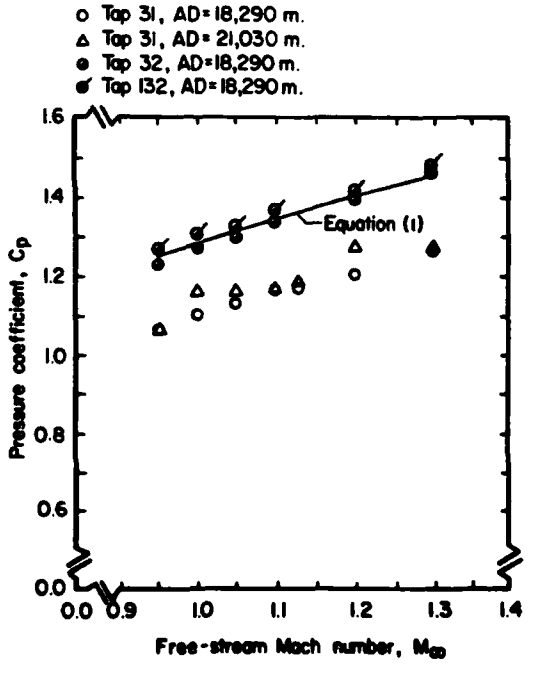

Figure 5. - Pressure coefficients for flat face as a function of free-stream Mach number.

faced portion of the nose cone. As a result, the static pressure decreases with r over the flat face from the "stagnation pressure" at the axis of symmetry to the sonic value at the corner. Using the data presented in Figure 4 (which are for $M_\infty = 2.01$), one would expect the local static pressure at $r = 0.90\ R_{ff}$ to be approximately $0.9\ p_{t2}$. As a result, the C_p for this orifice would be approximately 1.22 when $M_\infty = 1.3$. This value is in reasonable agreement with the data of Figure 5, considering the difference in the free-stream Mach numbers and the differences in the flow field due to the presence of the inlet hole.

3.1.2. Pressures on Conical Surface of Ogive

Additional information about the flow field can be determined from the schlieren photograph in Figure 3. Of interest is the flow over the first (forward) conical segment. A rapid expansion of the flow just past the corner is terminated by a shock wave near $x = 0.1\ x_o$. It is assumed that the shock wave results when the flow external to a separation bubble (which exists at the corner) turns when it reattaches to the surface. Furthermore, although the cavity (containing the exhaust ports) is relatively long, the flow appears to "jump over" the cavity; i.e., the cavity is open, since there is no recompression shock wave near the end of the cavity. However, the pressure data from the present tests indicate that the flow does not completely clear the cavity since the pressures indicate a (weak) recompression of the flow near the midpoint of the cavity.

The experimentally-determined C_p distributions for $M_\infty = 1.3$ at a density altitude of 18,290 m are presented in Figure 6. Included in Figure 6 is an outline of the configuration, showing pertinent geometric features. The detailed sketch of the geometry of the nose cone, Figure 2, illustrates the locations of the pressure taps and some features of a proposed model for the external flow. Although the flow expands rapidly around the corner, it cannot accelerate fast enough to remain attached to the surface, and a separation bubble forms at the corner. This assumption is supported by the pressure measured at the orifice in the "separated region" (at $x = 0.030\ x_o$) which is relatively low.

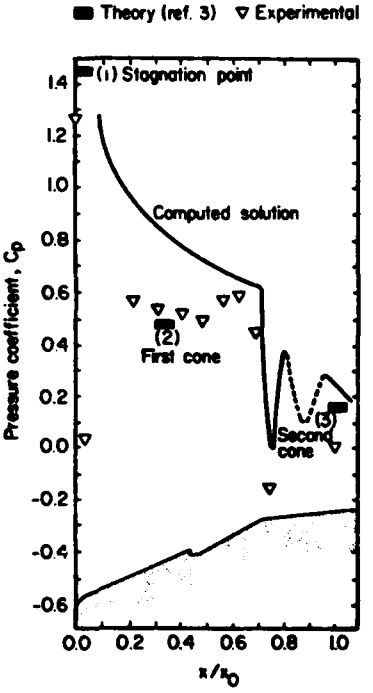

Figure 6. - Comparison between theoretical and experimental pressure distributions, $M_\infty = 1.3$, AD = 18,290 m.

Downstream of the separation bubble, the flow over the external surface of the nose cone was calculated using two different

approaches. Theoretical values of C_p were calculated using standard normal shock-wave tables and graphs for sharp cones. Values are presented

(1) for the stagnation point (C_p = 1.45),
(2) for the forward conical segment (C_p = 0.48, the value for a sharp cone whose half-angle is 20.5°), and
(3) for the second conical segment (C_p = 0.16, the value for a sharp cone whose half-angle is 10.75°).

Also included is the theoretical distribution computed using the University of Texas' Missile Aerodynamics Code, which is similar to that described by Moore and Swanson (4). In preparing the geometric input for the computer solution, the presence of the cavity in the external contour was omitted and the nose cone was represented by two conical frustums. Because of the extreme bluntness of the nose cone, the computed solution should be considered approximate.

Both the computed solution and the "sharp-cone" approximations (3) provide a reasonable estimate of the pressures on the downstream (second) conical segment, i.e., for $x \geq 0.716\ x_o$. The computer solution even predicts the rapid "overexpansion" that takes place downstream of the intersection of the two conical segments. An oscillatory character which appeared in the computed solution for the pressure distribution for the second conical segment is represented in Figure 6 by a broken line. The broken-line representation was used since the variation may be a computational peculiarity and not a flow phenomenon.

The most significant differences between the theoretical values and the experimental values occur on the forward conical surface and in the cavity in this region. Note that the upstream edge of the cavity is at $x = 0.423\ x_o$. The experimental pressures at the first tap of the cavity (tap 17 at $x = 0.482\ x_o$) are essentially equal to those upstream of the cavity. The fact that the pressure did not decrease when the flow separated at the cavity is attributed to the relatively shallow depth of the cavity. The pressure increase at the three pressure taps in the downstream region of the cavity ($0.551\ x_o \leq x \leq 0.689\ x_o$), reflects the recompression of the flow as it reattaches to the surface. Thus, if one assumes that a tangent-cone approximation is valid for the forward conical surface and that a recompression pressure rise occurs at the downstream end of the cavity, one can explain the fact that the pressures measured at the taps between $0.551\ x_o$ and $0.689\ x_o$ are above the Ames theoretical estimates (3). Since both theoretical models are approximate, close correlation with the data should not be expected. Each assumed model probably contains elements of the actual flow field.

The effect of M_∞ on the pressure distribution is illustrated by the data presented in Figure 7. This pressure distribution is for a density altitude of 21,030 m. There is a consistent trend with Mach number at all the orifices from $x = 0.030\ x_o$ to $x = 1.000\ x_o$. That is, the ratio p/p_{t2}

at a particular orifice decreases as the Mach number increases. The variation is greatest at the two extreme orifices. The Mach-number dependent variation at $x = 0.030\ x_o$ indicates a change in the characteristics of the separation bubble for these transonic flows. At the last orifice, the pressure ratio varies by almost a factor of two. However, the experimental values of p/p_{t2} at this orifice vary relatively little for $1.1 \leq M_\infty \leq 1.3$. Thus, the spread in the data for the three lowest Mach numbers suggests that a significant change occurs in the downstream region of the flow field for these transonic flows. But these transonic changes in the flow field occur far enough downstream (on the second conical segment) that they do not affect the flow through the fluidic generator.

To establish if this Mach-number-dependence has an analytical basis, let us examine the C_p as given by the small deflection approximation for supersonic flow,

$$C_p = \left(\frac{p}{p_\infty} - 1\right)\frac{2}{\gamma M_\infty^2} = \frac{C_1}{\sqrt{M_\infty^2 - 1}}, \qquad (2)$$

where C_1 is a constant (which is dependent on M_∞ and the local flow direction). The equation can be rearranged to yield:

$$\frac{p}{p_\infty} = \frac{\gamma C_1 M_\infty^2}{2\sqrt{M_\infty^2 - 1}} + 1 \quad . \qquad (3)$$

Rewriting this expression in terms of the pressure ratio used in Figure 7, we obtain

$$\frac{p}{p_{t2}} = \frac{p_\infty}{p_{t2}}\left(\frac{0.7 C_1 M_\infty^2}{\sqrt{M_\infty^2 - 1}} + 1\right). \qquad (4)$$

Using the Ames tables (3) to obtain the value of p_∞/p_{t2} as a function of Mach number, one finds the following values.

$$\frac{p}{p_{t2}} = 0.5595\ [0.7C_1(2.8903) + 1] \text{ for } M_\infty = 0.95$$

$$= 0.4689\ [0.7C_1(2.6402) + 1] \text{ for } M_\infty = 1.10$$

$$= 0.3685\ [0.7C_1(2.0345) + 1] \text{ for } M_\infty = 1.30.$$

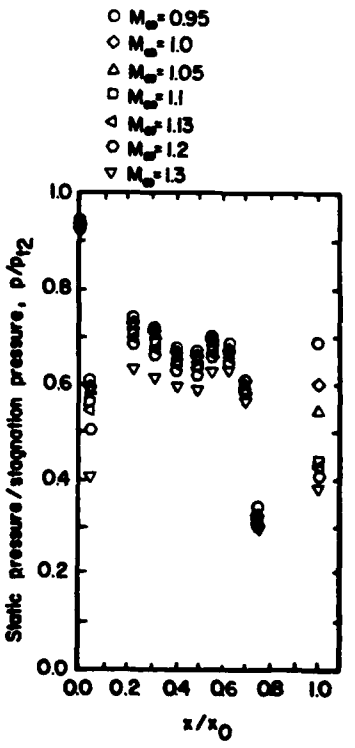

Figure 7. - Effect of Mach number on pressure distribution for AD = 21,030 m.

Using this relatively simple approximation, one would expect the pressure ratio p/p_{t2} to decrease with Mach number for these test conditions. Thus, although one would predict a greater decrease in the pressure ratio using equation (4) than is actually exhibited by the data, the small-deflection approximation provides a qualitative substantiation of the observed Mach-number dependence.

Although the pressures measured on the conical surface exhibit an inverse dependence on M_∞, the pressure ratio (p/p_{t2}) for locations on the blunt face should be independent of the Mach number for supersonic flows. The data from the orifice on the flat face (see the pressure measurements for x = 0.0, presented in Figure 7) exhibit this Mach-number independence.

3.2 Flow Through Fluidic Generator and Internal Pressure Measurements for 0° Angle of Attack

As has been discussed, the air which activates the fluidic generator enters the inlet hole in the stagnation region, passes through the resonator-interaction region of the generator assembly and then into the internal chamber, before it finally flows through the exhaust ports. A sketch of this internal flow pattern and of the relevant pressure instrumentation is presented in Figure 8. The mass-flow rate through the fluidic generator was calculated with the pressures measured at the orifices of Figure 8, using two different assumptions regarding the air flow through the fluidic generator.

Flow Model 1.--Because the area of the annular gap around the nozzle centerbody is so much less than the area of the inlet hole, the air velocity forward of the centerbody is relatively small. Thus, this region serves as a reservoir (or stagnation chamber) for the nozzle centerbody. The static pressures both at tap 25 ($x = 0.026\ x_o$) and at tap 26 ($x = 0.132\ x_o$) are essentially equal to p_{t2} over the entire range of Mach number and of density altitude.

It is assumed that the flow accelerates isentropically from this "reservoir" through the annular gap, reaching the speed of sound at the minimum cross-sectional area of the annular gap. Thus, the centerbody serves as a throat, "choking" the flow over the entire range of test conditions for this program. Fliegner's formula (5) for the choked flow of perfect air along with the minimum cross-sectional area of the annulus can be used to calculate the mass-flow rate, $\dot{m}_1$:

$$\frac{\dot{m}_1}{\rho_\infty U_\infty A_{In}} = \frac{0.0386[p(25)]}{\rho_\infty U_\infty \sqrt{T_t}} \quad , \tag{5}$$

where p(25) is the pressure at tap 25 (see Figure 2), ρ_∞ = free-stream density (kg/m^3), U_∞ = free-stream velocity (m/s), and T_t = stagnation temperature (K). The local mass-flow rate has been divided by $\rho_\infty U_\infty A_{In}$

(which is equal to the free-stream mass-flow rate across an area equal to that of the inlet hole) in order to obtain a dimensionless parameter, which is independent of the Mach number and of the density altitude over the range of test conditions.

Because the air must go around the corner of a flat-faced cylinder as it enters the nozzle centerbody (producing a separation bubble) and because of the presence of boundary layers on both surfaces of a narrow annular gap, it is expected that the effective throat area is significantly less than the minimum cross section of the annular gap (which is the area used in eq. (5)). Thus, it is expected that the non-dimensionalized values of $\dot{m}_1$, as calculated using equation (5) (which are represented by the half-filled symbols of Figure 9), overestimate the actual mass-flow rate.

It is believed that the flow is indeed choked by the nozzle centerbody, even though the static pressures in the (downstream) internal chamber are approximately 0.7 p_{t2}. The reason for the chamber value of 0.7 p_{t2} follows. The pressure in the internal chamber is governed (1) by the pressure in the external cavity (which is established by the external flow field), since (as will be discussed) the flow through the exhaust ports is not choked, and (2) by the pressure drop across the exhaust ports, which is governed by the mass-flow rate, as shown in equation (6a). The mass-flow rate is established by the choking of the flow through the

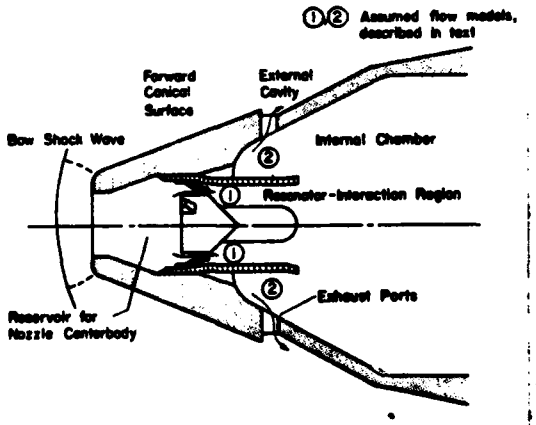

Figure 8. - Nomenclature for flow models.

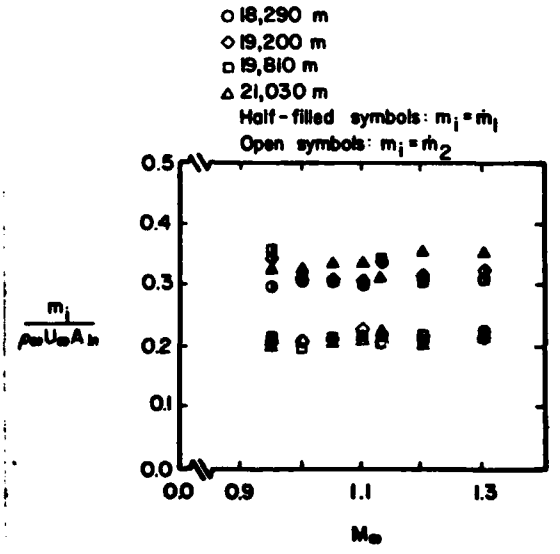

Figure 9. - Mass-flow rate through fluidic generators.

nozzle centerbody. The static pressure increases from the sonic value (0.53 p_{t2}) at the throat of the nozzle centerbody to 0.7 p_{t2}, the value in the internal chamber, as it flows through the resonator-interaction region of the generator assembly (see Figures 1 and 8) and into the internal chamber.

The conclusion that the flow is choked not at the exhaust ports but at the nozzle centerbody over the range of test conditions is very important. It has been shown that the pressure ratio (p/p_{t2}) for the separated region of the external cavity is a well-behaved function of the free-stream Mach number and is independent of density altitude. Since the pressure drop across the exhaust ports is relatively small and is a function of the mass-flow rate through the fluidic generator, the pressure in the internal chamber (which is the "back pressure" for the resonator-interaction region of the fluidic generator) follows the external pressure. However, since the flow is choked by the nozzle centerbody, the inlet pressure for the resonator-interaction region is a fixed fraction of p_{t2} (i.e., 0.53, the sonic value). It is expected that the details of the flow field in the resonator depend on the pressure differences across it.

Flow Model 2.--For the second flow model, the volumetric flow-rate, Q, was calculated using the equation for subsonic flow through a sharp-edged, circular orifice (6):

$$Q = 0.6YA\sqrt{\frac{2\Delta p}{\rho}} \quad , \tag{6a}$$

where for the orifice ratios and for the Reynolds numbers of the present tests,

$$Y = \left\{1.0 - 0.3\ \frac{\Delta p}{p_1}\right\} \quad . \tag{6b}$$

Furthermore, it is assumed that the acceleration of the flow from the internal chamber through the exhaust ports is such that

$$\rho \propto p \quad . \tag{6c}$$

Combining these relations, one can calculate the mass-flow rate for this model using the relation

$$\frac{\dot{m}_2}{\rho_\infty U_\infty A_{In}} = \frac{0.158\ p(16)}{\rho_\infty U_\infty \sqrt{T_t}} \left\{0.7 + 0.3\ \frac{p(16)}{p(27)}\right\} \sqrt{1.0 - \frac{p(16)}{p(27)}} \quad . \tag{7}$$

The mass-flow rates thus calculated are presented as a function of M_∞ in Figure 9 (as the open symbols). The experimentally determined values of the pressure ratio [p(16)]/[p(27)] indicate that the flow in this region is incompressible. Thus, the assumptions made in developing flow model 2 are quite realistic. Since the two pressures needed to

calculate the flow field were measured directly, it is believed that the mass-flow rates calculated using equation (7), i.e., $\dot{m}_2$, are the more realistic of the two flow models.

4. CONCLUSIONS

This analysis showed that pressures measured at the inlet hole to the fluidic generator are in close agreement with those given by normal shock relations. Over the external surface of the ogive, the ratio of local static pressure to stagnation pressure measured at the nose, p/p_{t2} decreased as the free stream Mach numbers increased. Within this trend existed regions of expansion and compression which were a result of the ogive's geometry and the injection of the air exhausted from the fluidic generator. Theoretical models predicted reasonably well the dependence on Mach numbers of p/p_{t2} as well as the relative values of p/p_{t2} at different points on the ogive. Pressures measured at the entrance and exit of the region occupied by the generator permitted calculation of the mass flow rate through the fuze. This analysis verified that the key factors that should be duplicated in laboratory tests were the pressures at the generator's entrance and at the exhaust ports in the ogive; but the most significant result was the accumulation of a data base of the actual pressures to be associated with desired combinations of Mach number and altitude. Consequently, the high altitude chamber proposed to test MLRS fuzes has been incorporated into the product specification and used with confidence in the quality assurance program of the contractor.

LITERATURE CITED

1. R. L. Goodyear and H. Lee, Performance of the Fluidic Power Supply for the XM-445 Fuze in Supersonic Wind Tunnels, HDL-TM-81-4, Feb. 1981, Harry Diamond Laboratories.

2. J. C. Boison and H. A. Curtiss, An Experimental Investigation of Blunt Body Stagnation Point Velocity Gradient, ARS Journal, Feb. 1959, Vol. 29, No. 2, pp. 130-135.

3. Ames Research Staff, Equations, Tables, and Charts for Compressible Flow, Report 1135, 1953, NACA.

4. F. G. Moore and R. C. Swanson, Jr., Aerodynamics of Tactical Weapons to Mach Number 3 and Angle of Attack 15°, Part I--Theory and Application, NSWC/DL TR-3584, Feb. 1977, Naval Surface Weapons Center.

5. A. H. Shapiro, The Dynamics and Thermodynamics of Compressible Fluid Flow, Ronald Press, New York, 1953.

6. Staff, Flow of Fluid Through Valves, Fittings, and Pipes, Technical Paper No. 410, The Crane Company.